

Interspecies-chimera machine vision with polarimetry for real-time navigation and anti-glare pattern recognition

Received: 29 November 2023

Accepted: 1 August 2024

Published online: 07 August 2024

 Check for updatesTao Guo^{1,2}, Shasha Li¹, Y. Norman Zhou², Wei D. Lu³, Yong Yan^{1,2,4}✉ & Yimin A. Wu²✉

Cutting-edge humanoid machine vision merely mimics human systems and lacks polarimetric functionalities that convey the information of navigation and authentic images. Interspecies-chimera vision reserving multiple hosts' capacities will lead to advanced machine vision. However, implementing the visual functions of multiple species (human and non-human) in one optoelectronic device is still elusive. Here, we develop an optically-controlled polarimetry memtransistor based on a van der Waals heterostructure (ReS₂/GeSe₂). The device provides polarization sensitivity, nonvolatility, and positive/negative photoconductance simultaneously. The polarimetric measurement can identify celestial polarizations for real-time navigation like a honeybee. Meanwhile, cognitive tasks can be completed like a human by sensing, memory, and synaptic functions. Particularly, the anti-glare recognition with polarimetry saves an order of magnitude energy compared to the traditional humanoid counterpart. This technique promotes the concept of interspecies-chimera visual systems that will leverage the advances of autonomous vehicles, medical diagnoses, intelligent robotics, etc.

The global market of machine vision was validated at USD 16.89 billion in 2022, which is expanding with an annual growth rate of 12.3% (2023–2030)¹. Machine visions are profoundly prevailing in autonomous vehicles, medical diagnosis, video processing, iris encryption, cyborgs, etc. However, traditional visual systems are bulky, energy-intensive, and lengthy, especially for cognitive tasks owing to discrete computation hierarchy². The sensory, memory, and computing units are separated from each other. The location and format (analog/digital) of image data need to be changed frequently, rising the penalty of energy consumption and time delay (Fig. 1a). To solve this issue, mimicking human visual systems is a promising strategy^{3,4}. In human visions, photoreceptors and neurons in the human retina detect and pre-process images that are later sent to the visual cortex for cognitive signal processing. For current cutting-edge machine visions, intelligent

photodetectors can simultaneously sense and pre-process light stimuli like a human retina^{5,6}. Received images are then directly transferred into artificial neural networks (ANNs) for complex visual processing. ANNs fundamentally imitate the fundamental principles of human brains relying on the activities of synapses and neurons, which can realize huge parallel computing and high-energy efficiency (Fig. 1b)^{7,8}. However, human eyes only provide very limited photodetection abilities regarding the light wavelength (380 nm to 700 nm), intensity (comfortable intensity for human eyes: 200 lux to 750 lux), and vector (not sensitive to linear and circular polarity)^{9,10}. This significantly restrains the application of cutting-edge humanoid machine vision. Notably, interspecies-chimera machine vision seamlessly integrates the cognitive function of humans and the special visual function of other species (Fig. 1c). This can leverage functions beyond traditional artificial intelligence (AI).

¹School of Physics, Henan Normal University, Henan 453007, China. ²Department of Mechanical and Mechatronics Engineering, and Waterloo Institute of Nanotechnology, Materials Interfaces Foundry, University of Waterloo, Waterloo, ON N2L 3G1, Canada. ³Department of Electrical and Computer Engineering, the University of Michigan, Ann Arbor, MI 48109, USA. ⁴iGaN Laboratory, School of Microelectronics, University of Science and Technology of China Hefei, Anhui 230026, China. ✉e-mail: yanyong@htu.edu.cn; yimin.wu@uwaterloo.ca

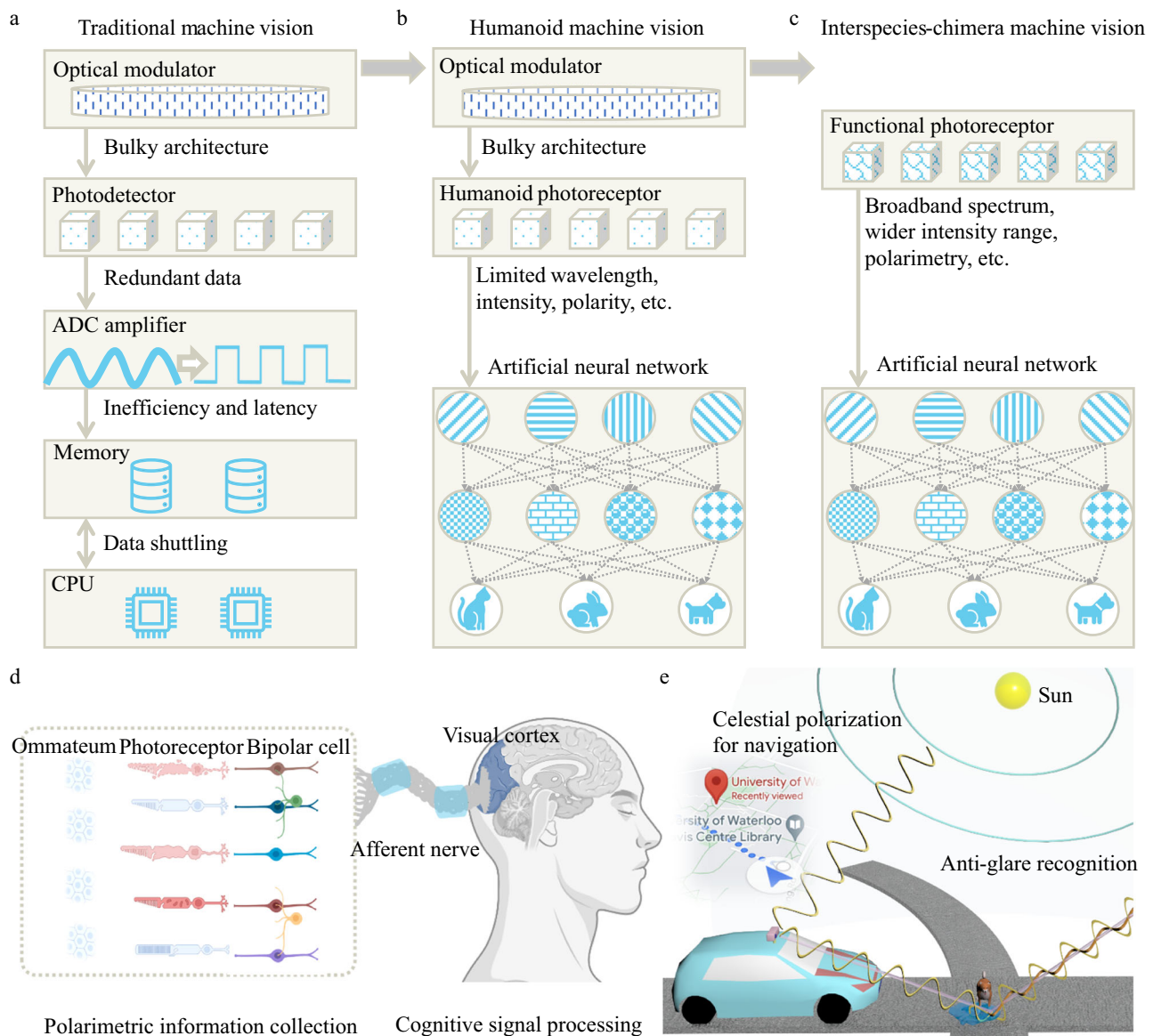


Fig. 1 | Interspecies-chimera machine vision. **a** The architecture of traditional machine vision systems. The system is bulky with separated sensing, analog-to-digital converter (ADC), memory, and computing units, resulting in a high energy budget and slow computing speed. **b** The architecture of humanoid machine vision systems. The system shows limited sensing ability, including the narrow bandwidth, small margin of signal density, and lack of polarimetric sensitivity. **c** The architecture of

interspecies-chimera machine vision systems. This can complete cognitive tasks like the intelligence species of humans and other functions. **d** Schematic of an interspecies-chimera visual system. It integrates the ommatidium from the honeybee and the cognitive visual cortex from human beings. **e** Schematics of an application scenario of autonomous vehicles with the interspecies-chimera machine vision. Real-time navigation and anti-glare recognition can be achieved simultaneously.

Machines solve problems like humans while possessing super-human capabilities enabled by other appealing functions¹¹.

Humanoid machine vision has been reported to reduce background noise¹², scotopic/photopic adaptation¹³, broadband sensing^{14,15}, convolution processing^{16,17}, etc. In the human vision system, the image information is received and pre-processed by the retina and transferred into the visual cortex region for cognitive processing (Fig. 1d)¹⁸. Human vision, although, is capable of cognitive tasks. It is not sensitive to the polarization of light which includes critical information¹⁹. It is rudimentary to integrate polarimetric functions into humanoid machine vision. Honeybees are known as excellent navigators with the help of ommatidium measuring polarized lights. The skylight pattern is determined by the position of the sun, described by the Rayleigh sky model (Supplementary Fig. 1)²⁰. For instance, real-time navigation can be achieved via monitoring the sun-position-related celestial polarization cues²¹. Indeed, the polarimetric capability makes honeybees a

master for navigating from the honeycomb to a flower patch. But honeybees are not intelligent species like humans. Therefore, a rational design philosophy is to integrate the polarimetry from honeybees and the intelligence from humans, creating an interspecies-chimera machine vision (Fig. 1d). Particularly, the reflected light from shiny surfaces, including cars' windows, buildings, water on the road, and the road itself, forms glare spots. This compromises the processing accuracy in traditional machine visions due to glare-induced distortion²². The formation of glare spots is because the reflected light is partially polarized light parallel to the surface. The polarimetric function can suppress the light intensity with a certain polarization (glare spots) and keep high fidelity in authentic images. One of the promising applications of the design is autonomous vehicles (Fig. 1e). This interspecies-chimera machine vision, on the one hand, can detect the polarization pattern in the sky for real-time navigation. On the other hand, the system can realize anti-glare pattern recognition.

Van der Waals (vdW) heterostructures are promising for optical sensing, memory, and computing. Two-dimensional (2D) materials have excellent optoelectronic properties, atomically thin thickness, high-carrier mobility, and tuneable electrical transports²³. In particular, 2D materials with in-plane anisotropic structures can realize polarimetric functions to lights²⁴. Although other materials are also sensitive to polarized lights, such as metamaterials²⁵, anisotropic halide perovskites²⁶, anisotropic and polymer crystals²⁷. 2D polarimetric devices utilizing atomic-level anisotropy are compatible with complementary metal-oxide semiconductor (CMOS) fabrication techniques. They have the potential to realize high-density integration and excellent scalability²⁸. Furthermore, 2D materials exhibit good memory, and computing capabilities, which are easier to fuse with polarimetry functionalities²⁹. Multi-terminal memtransistors based on vdW heterostructures can achieve programmable optoelectronics and complex functions of hetero-synaptic plasticity that can be used for brain-inspired neuromorphic computing^{30,31}.

Among the 2D materials library, ReS₂ and GeSe₂ with excellent optoelectronic properties have been employed for memory and neuromorphic vision systems. Mo-irradiated ReS₂ (Mo-ReS₂) showed promising resistive switching under electronic stimuli³². Photoconductivity was also investigated in ReS₂-based devices, indicating the potential for machine vision³³. Interestingly, the polarization sensitivity of ReS₂ was also investigated for neuromorphic vision with 3D visual polarization imaging and visual adaptation abilities^{34,35}. Previous work has also confirmed the good performance of GeSe₂ due to excellent photosensitivity and charging conducting features^{36,37}. Resistive switching behaviors that are crucial to neuromorphic computing systems were observed in GeSe₂³⁸. The tuneable electrical properties and photosensitivity make the two materials desirable for machine visions. Optical-controlled 2D devices for machine vision have been summarized (Supplementary Table 1). A multifunctional device with polarization sensitivity, long-term nonvolatility, and positive/negative reconfigurable photoconductance simultaneously has few investigations and is very promising. This can seamlessly integrate polarization sensitivity, light sensing, memory, and neuromorphic computing, which will leverage AI applications.

In this work, a vdW heterostructure device employing 2D ReS₂ and GeSe₂ with anisotropic structures was developed. The optically-controlled polarimetry memtransistor (OCPM) can realize optically-programmed non-volatile states and has the sensitivity to polarized lights. Both positive photoconductivity (PPC) and negative photoconductivity (NPC) under the light of 808 nm and 405 nm were obtained respectively. This can achieve continuous transition and a similar conductance range in both potentiation and depression operations, demonstrating better computing accuracy (Supplementary Fig. 2). The behaviors mimicked the antagonistic shunting and memory of bipolar cells, demonstrating the sensing function of the retina and the computation function of the visual cortex. The conductance of the device can be gradually increased and decreased by light stimuli, corresponding to long-term potentiation and depression. This can be used to construct artificial neural networks (ANNs) for neuromorphic computing. The polarization sensitivity was used for real-time navigation inspired by honeybees. Experimental values were consistent with actual values, indicating practicable accuracy. Besides, the polarimetry was integrated with cognitive neuromorphic seamlessly to realize anti-glare pattern recognition. The OCPM array with anti-glare abilities decreased the energy budget to 11% compared to the neuromorphic vision without polarimetry. This interspecies-chimera machine vision provided a concept to design AI systems and will benefit autonomous vehicles, medical diagnoses, holography techniques, intelligent robotics, etc.

Results

Materials characterizations of OCPM device

The stacked ReS₂/GeSe₂ layers were employed to construct the OCPM (Fig. 2a). The source-drain current (*I*_{ds}) flowed along the b-axis

direction of both ReS₂ and GeSe₂ layers^{39,40}. The ReS₂ has a distorted 1T structure deriving from a hexagonal structure (Supplementary Fig. 3). Meanwhile, GeSe₂ is the two-dimensional crystal with the monoclinic crystal structure (Supplementary Fig. 4). ReS₂ and GeSe₂ have in-plane anisotropic structures and direct bandgaps, indicating excellent bi-axial optical and electrical properties^{41,42}. Polarization-sensitive absorption spectra were measured to further investigate the bi-axial optical properties. In the experimental setup (Supplementary Fig. 5), a linear polarizer was utilized to polarize the irradiated light. For the initial state (rotation angle = 0°), the polarization direction of irradiated light was parallel with the b-axis direction of measure materials. To acquire the polarization-sensitive absorption spectra mapping, the sample was rotated clockwise by an angle of 10° for each step. Polarization-sensitive absorption spectra mapping of the ReS₂ layer was recorded (Fig. 2b). The results presented an angle-dependent absorption feature, indicating linear dichroic effects⁴³. Notably, exciton absorption peaks at around 800 nm were observed when the rotation angles were 0° and 180° compared to the 90° and 270° counterparts⁴⁴. Typical polarization-sensitive absorption spectra of ReS₂ under the rotation angle of 0° and 90° were extracted (Supplementary Fig. 6). A higher absorption coefficient was observed when the polarized light was parallel with the b-axis of ReS₂ ([010] direction of the ReS₂ crystal) compared to the perpendicular counterpart. Besides, the blueshift feature of absorption spectra was found when the rotation angle increased from 0° to 90° (Supplementary Fig. 6). This implied the anisotropic electronic properties. The polarization-sensitive absorption spectra mapping of the GeSe₂ layer was also measured (Fig. 2c). An angle-dependent absorption feature was presented with linear dichroic effects. Typical polarization-sensitive absorption spectra of GeSe₂ under the rotation angle of 0° and 90° were extracted (Supplementary Fig. 7). The material showed higher absorption ability when the polarized light was parallel with the b-axis of the GeSe₂. The bi-axial optoelectronic properties of ReS₂ and GeSe₂ are the fundamentals of polarimetric capabilities.

To confirm the anisotropic characteristic of ReS₂ and GeSe₂, the Raman spectra of the materials were measured. The typical Raman spectrum of the ReS₂/GeSe₂ double layer was shown (Supplementary Fig. 8). The observed peaks all belong to the used materials as labeled. The peak located at 520 cm⁻¹ was attributed to the substrate of Si. The typical peaks of ReS₂ were located at 149 cm⁻¹ and 209 cm⁻¹ corresponding to the in-plane E_g mode and A_g¹ modes respectively⁴⁵. The A_g¹ mode of GeSe₂ was found at 194 cm⁻¹⁴⁶. The angle-resolved polarized Raman spectra of the ReS₂/GeSe₂ bi-layer were measured for investigating anisotropic properties (Fig. 2d). The ReS₂/GeSe₂ vdW heterostructure with aligned b-axis direction was placed on a SiO₂/Si substrate (Supplementary Fig. 9). The b-axis direction of stacked GeSe₂/ReS₂ layers was parallel with the polarized light at the beginning (rotation angle = 0°) of the measurement. Then the sample was rotated by the step of 10° (GeSe₂/ReS₂ layers rotate together). The corresponding Raman spectra were collected at each step. The angle-resolved polarized Raman spectra mapping is depicted (Fig. 2d). Raman signal amplitudes changed periodically with the increased rotation angles, meaning an anisotropic structure in the in-plane dimension⁴⁷. The classical Placzek model gave an insight understanding to the anisotropic structure. The Raman signal intensity is described by the following equation⁴⁸:

$$S \propto |\mathbf{e}_i \cdot \mathbf{R} \cdot \mathbf{e}_s|^2 \quad (1)$$

where *S* is the Raman signal intensity, *e_i* is the unit polarization vectors described by Eq. (2):

$$\mathbf{e}_i = [0 \cos \theta \sin \theta] \quad (2)$$

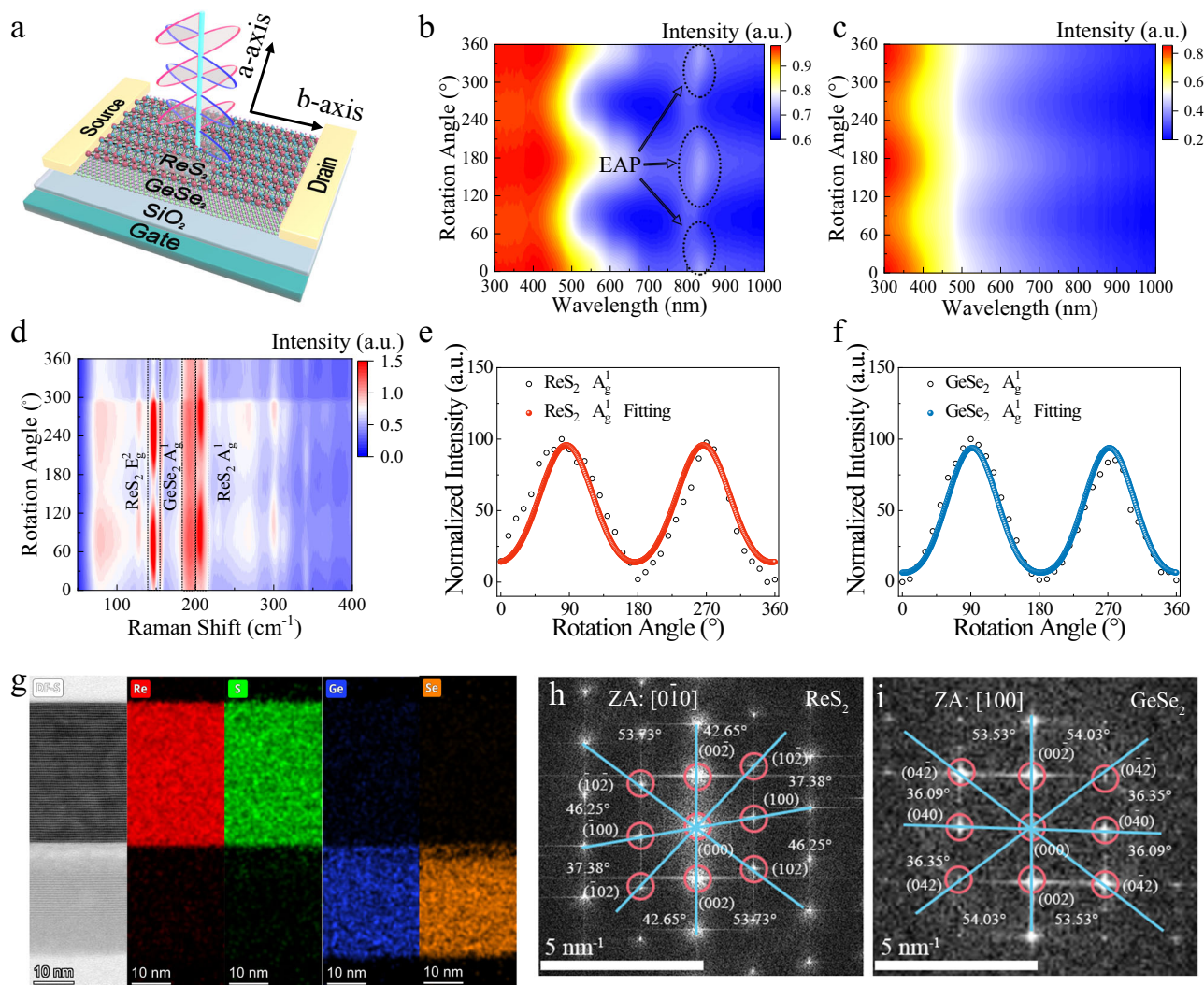


Fig. 2 | Material characterizations of OCPM device. **a** Schematic diagram of the OCPM. **b** Polarization-sensitive absorption spectra mapping of the ReS₂ layer. EAP means exciton absorption peak. The rotation angle is with respect to the b-axis in-plane clockwise. **c** Polarization-sensitive absorption spectra mapping of the GeSe₂ layer. The rotation angle is with respect to the b-axis in-plane clockwise. **d** Typical angle-resolved polarized Raman spectra mapping of the ReS₂/GeSe₂ bi-layer. **e** The

angle-dependent Raman intensity of the A_g¹ mode for ReS₂. **f** The angle-dependent Raman intensity of the A_g¹ mode for GeSe₂. **g** The cross-section of the ReS₂/GeSe₂ bilayer and the corresponding element distribution. **h** The fast Fourier transform (FFT) pattern of ReS₂. ZA means zone axis. **i** The fast Fourier transform (FFT) pattern of GeSe₂.

R represents the Raman tensor described as a 3×3 matrix⁴⁹:

$$\mathbf{R} = \begin{bmatrix} a & 0 & 0 \\ 0 & b & 0 \\ 0 & 0 & c \end{bmatrix} \quad (3)$$

e_s means the unit polarization vectors of scattered Raman signals under the parallel or cross-polarization modes. The parallel mode was used in this work, which is described as Eq. (4):

$$\mathbf{e}_{s\parallel} = |0 \cos\theta \sin\theta|^T \quad (4)$$

where θ gives the rotation angle. The angle-dependent Raman signal intensity for A_g mode under the parallel working mode is described by Eq. (5):

$$S_{A_g}^{\parallel} \propto |b \cos^2 \theta + c \sin^2 \theta|^2 \quad (5)$$

The angle-dependent Raman intensity of the A_g¹ mode was studied. The experimental and fitting plots of ReS₂ (Fig. 2e) and GeSe₂ (Fig. 2f) are presented. Notably, the experimental data points are fitted well with theoretical values. A signature periodic variation feature of 180° was observed for both ReS₂ and GeSe₂ (Fig. 2e, f). This clearly demonstrating a bi-axial anisotropic structure⁵⁰. Besides, the angle deviation of the two materials' orientation (b-axis direction) was merely 6°, which indicates very good alignment.

The thickness of ReS₂ and GeSe₂ layers were identified by the Atomic Force Microscopy (AFM) (Supplementary Figs. 10 and 11). The thickness of ReS₂ and GeSe₂ for constructing the OCPM were approximately 42 nm and 34 nm, respectively. Meanwhile, the high-angle annular dark-field (HAADF) image was measured to analyze the cross-section of the stacked ReS₂/GeSe₂ structure (Fig. 2g). The laminate structure was observed in both ReS₂ and GeSe₂ layers. The Re, S, Ge, and Se were distributed uniformly in the corresponding regions in the energy dispersive X-ray spectroscopy elemental mapping (Fig. 2g). No other impurity elements were found (Fig. 2g). The HAADF atomic scale image of ReS₂ indicated a high crystallinity of

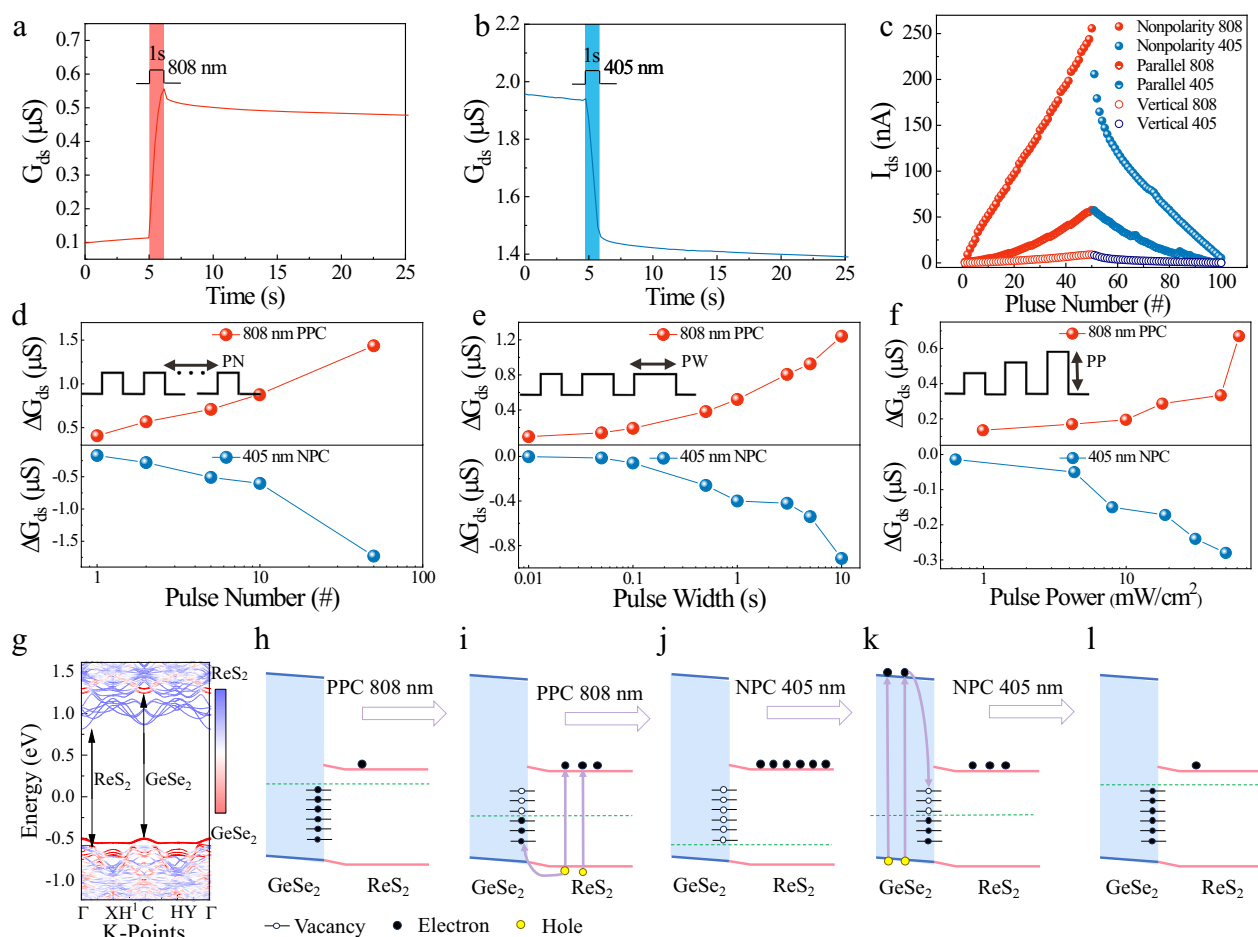


Fig. 3 | Optoelectronic properties and working mechanism of $\text{ReS}_2/\text{GeSe}_2$ heterostructures OCPM. **a** I-t curve demonstrating non-volatile PPC ($V_{\text{gs}} = -10$ V). The illumination intensity of 808 nm wavelength was fixed as $19 \text{ mW}/\text{cm}^2$. This power was used for all the rest of PPC operations without special instructions. **b** I-t curve demonstrating non-volatile NPC ($V_{\text{gs}} = -10$ V). The intensity illumination with 405 nm wavelength was fixed as $19 \text{ mW}/\text{cm}^2$. This power was used for all the rest of NPC operations without special instructions. **c** Fully optical-controlled

potentiation/depression with polarimetric functions (Light pulse width 10 ms, $V_{\text{gs}} = -10$ V, $V_{\text{ds}} = 0.1$ V). **d** Photocurrent changes (ΔI_{ds}) under different light PNs. **e** Photocurrent changes (ΔI_{ds}) under different light PWs. **f** Photocurrent changes (ΔI_{ds}) under different light PP. **g** Density functional theory calculated band structure of the $\text{ReS}_2/\text{GeSe}_2$ heterojunction. **h–l** The schematic diagram of the physical mechanism underlying the PPC and NPC performances.

the exfoliated ReS_2 (Supplementary Fig. 12). The interlayer spacing was approximately 0.64 nm along the $[001]$ direction. The atomic scale HAADF image of GeSe_2 also demonstrated a crystalline feature with the interlayer spacing of 0.59 nm (Supplementary Fig. 13). Meanwhile, the fast Fourier transform (FFT) patterns were obtained to get more insight into crystalline structures. In the FFT pattern of ReS_2 crystalline, clear spots were observed in the reciprocal space (Fig. 2h), indicating the single crystalline structure. The FFT spots were consistent with the distorted 1T structure⁵¹. The angle between $(00\bar{2})$ and $(10\bar{2})$ reflections in ReS_2 was 53.73° which was 11.08° deviating from the angle between $(00\bar{2})$ and $(10\bar{2})$ reflections (42.65°). The angle between crystal planes reflections of $(00\bar{2})$ and (100) in ReS_2 was 99.98° which was 19.95° bigger than that of $(00\bar{2})$ and (100) (80.03°)⁵². This confirmed a strong in-plane anisotropy⁵³. Meanwhile, the corresponding FFT pattern along the $[100]$ zone axis of GeSe_2 was detected (Fig. 2i). The monoclinic $\beta\text{-GeSe}_2$ was identified by the FFT pattern³⁷. The angle between crystal planes reflections of $(00\bar{2})$ and (040) was 89.62° , which was smaller than that of $(00\bar{2})$ and (040) (90.38°), demonstrating an anisotropic structure⁴². Both optical spectra and atomic structure anisotropies of ReS_2 and GeSe_2 were characterized, which are the fundamentals of bi-axial optoelectronics in the OCPM.

Optoelectronic properties and working mechanism of OCPM

Optoelectronic properties and working mechanism of the OCPM have been systematically investigated. The light-wavelength-dependent transfer curves (Supplementary Fig. 14) were measured to identify the operation gate voltage. The light illuminations with the wavelengths of 405 nm and 808 nm were applied to the OCPM individually. The light power was low to avoid potential photo-induced defects⁵⁴. The device was only exposed to the power density lower than $100 \text{ mW}/\text{cm}^2$ referring to light sensing application based on GeSe_2 and ReS_2 ^{34,35,37,55}. The gate voltage effectively modulated the photoconductivity under illumination with different wavelengths. Both positive photocurrents and negative photocurrents were observed with respect to the dark current under a certain gate voltage slot (approximately -14.1 V to 1.4 V) as marked by a gray area (Supplementary Fig. 14). This enabled fully optical-controlled information processing with artificial neural networks (ANN)⁵⁶. The $I_{\text{ds}}-V_{\text{ds}}$ photocurrent output trace has been measured (Supplementary Fig. 15). It showed both positive and negative photo responses under different light illuminations. The source-drain currents increased with the increase of gate voltage, demonstrating the n-type characteristic in the channel⁵⁷. The I-t plot under an unpolarized pulsed light stimulation (808 nm wavelength) indicates non-volatile positive photoconductivity (PPC) properties (Fig. 3a). The initial conductance was different before the

shining of light (Fig. 3a vs 3b). The G_{ds} increased quickly as the light shining (808 nm) on the device. Particularly, the current remained at a larger value than the original dark state value after turning off the light illumination. This is a signature character of non-volatile functions⁵⁸. In comparison, after the device was programmed to the high conductivity by 808 nm, the conductance decreased when the light with the wavelength of 405 nm was shined on the device, and the lowered conductance was remained after the illumination, which meant the non-volatile negative photoconductivity (NPC) (Fig. 3b). This phenomenon indicated a non-volatile negative photoconductivity (NPC). The retention time of the device programmed by pulsed light was measured (Supplementary Fig. 16). The programmed currents remained for approximately 1000 s without any signs of degeneration. The co-existence of non-volatile PPC and NPC shows promising prospects for cognitive information processing based on ANNs⁵⁹. The output currents can be modulated gradually, corresponding to potentiation and depression behaviors (Fig. 3c). The programmable conductance can represent synaptic weights in ANNs, implementing the matrix-vector multiplication (MVM) for deep learning algorithms. The architecture used lights to program synaptic weights. The photonic device increases processing speed owing to high bandwidth, lowered parasitic crosstalk, and achieves ultralow power consumption comparing with electrical counterpart⁶⁰. Minimizing the asymmetric nonlinearity (ANL) of weight updating (potentiation/depression) is crucial for computing accuracy. A small ANL of 0.19 was obtained in the OCPM (Supplementary Fig. 17)⁶¹. The feature was comparable with the electronic-controlled artificial synapses⁶². Meanwhile, further analysis on potentiation/depression programming was implemented^{63–65}. The typical non-volatile conductance changes were programmed by light pulses (Supplementary Fig. 18a). The ΔG versus G_0 over 30 cycles were plotted. ΔG is the increase/decrease of conductance under light illumination, and the G_0 is the initial state before the programming operations^{63,64}. The potentiation and depression are depicted (Supplementary Fig. 18b, c). The inset shows the Normal Probability Plot. The mean value μ of the potentiation and depression were 7.16266 and -7.86515 respectively, demonstrating a near-symmetric feature. The standard deviation (σ) was 5.46145 and 6.67841 for potentiation and depression respectively. The device was operated for over 30 cycles without obvious variation of conductance (Supplementary Fig. 19a). Furthermore, the optoelectronic performances of fresh and three-month-old parts were compared (Supplementary Fig. 19b). A negligible difference was observed, indicating the excellent stability of the device. In particular, the OCPM also endowed polarization-sensitive potentiation/depression abilities (Fig. 3c). This can realize image preposing with polarimetric functions and in-sensor computing simultaneously, which goes beyond traditional humanoid machine vision.

Moreover, conductance modulations under multiple optical pulses with different pulse numbers (PN), pulses widths (PW), and pulse power (PP) were characterized (Fig. 3d–f). Identical neurological responses to different stimuli are essential in biological brains associating to learning and memory⁶⁶. More stimuli, higher frequent stimuli, and stronger stimuli trigger more intensive or more suppressive neurological responses and feedback. Bidirectional synaptic excitation and inhibition are the foundation for information processing in brains. Pyramidal cells in the primary visual cortex need to equalize excitation/inhibition ratios for visualization tasks⁶⁷. Conductance changes (ΔG_{ds}) under different light PNs were tested (Fig. 3d). The absolute ΔG_{ds} increased monotonically with the increase of PNs (PN from 1 to 50). The ΔG_{ds} of PPC increased from 0.41 μS to 1.44 μS (Fig. 3d). The absolute ΔG_{ds} of NPC increased from 0.17 μS to 1.73 μS , which indicates spike-number-dependent plasticity (SNDP) mimicking biological systems (Fig. 3d). Meanwhile, the PPC induced by 808 nm light was more obvious with longer pulse widths (PW varied from 10 ms to 10 s) (Fig. 3e). ΔG_{ds} was 0.1 μS under the shining of a 10 ms pulse (Fig. 3e). In comparison, ΔG_{ds} enlarged to 1.24 μS with a pulse width of 10 s (Fig. 3e). The 405 nm light also induced SRDP phenomena regarding the NPC behavior. The absolute values of ΔG_{ds}

increased from 0.02 μS (PW of 10 ms) to 0.92 μS (PW of 10 s) (Fig. 3e). The limit of response speed was evaluated by shining the 808 nm light with the pulse width of 0.1 ms (Supplementary Fig. 20). 0.1 ms was the fastest optical pulse that is limited by our current equipment. The non-volatile optical response can be potentially faster. The device can be potentially faster. Besides, the mimicking of biological spike-amplitude-dependent plasticity (SADP) was studied (Fig. 3f). Typical PP-dependent increase of ΔG_{ds} was measured. The ΔG_{ds} of PPC changed from 0.14 μS (1 mW/cm²) to 0.67 μS (61.9 mW/cm²) (Fig. 3f). Meanwhile, the absolute ΔG_{ds} of NPC changed from 0.14 μS (0.6 mW/cm²) to 0.28 μS (499 mW/cm²) (Fig. 3f). The light power dependent photocurrent ($I_{ph} = I_{light} - I_{dark}$)⁶⁸ for both PPC (808 nm) and NPC (405 nm) has been measured (Supplementary Fig. 21). Both NPC and PPC showed increased $Abs(I_{ph})$ under higher light density. The linear dynamic range (LDR) was calculated as 35.78 dB and 37.89 dB for PPC and NPC respectively. The influence of light intensity on the responsivity and detectivity was characterized (Supplementary Fig. 22). For the PPC under the illumination of 808 nm, the responsivity decreased from 22.24 A/W to 1.77 A/W when the light density decreased from 0.78 mW/cm² to 48.62 mW/cm² (Supplementary Fig. 22a). The highest and lowest detectivity of 2.91×10^{10} Jones and 2.31×10^9 Jones were measured under the highest and lowest illumination respectively (Supplementary Fig. 22b). The sensitivity was tending to the saturation status under higher incident intensity. Similar features were observed under the illumination of 405 nm. The highest responsivity of 35.90 A/W was observed when the light density was 0.5 mW/cm² (Supplementary Fig. 22c). The lowest responsivity (9.16 A/W) was obtained under the high-power illumination (39.21 mW/cm²). Meanwhile, the detectivity decreased from 8.64×10^9 Jones to 2.20×10^9 Jones when the power decreased (Supplementary Fig. 22d). Besides, the 405 nm light can achieve positive photoconductivity by modulating the gate voltage (Supplementary Fig. 23). The tuneable PPC and NPC responses in the OCPM provided more operational freedoms for sensing, memory, and bio-inspired neuromorphic computing. The endurance of the OCPM was tested by programming the device with electronic stimuli (Supplementary Fig. 24). The high resistance state (HRS) and low resistance state (LRS) were achieved by applying a positive gate voltage pulse and a negative gate voltage pulse, respectively. No degradation was observed after 10,000 switching cycles, demonstrating excellent reliability. The retention time of the programmed states was longer than 3000 s (Supplementary Fig. 25).

The working mechanism of the OCPM has been investigated. Two reference devices with a single layer of ReS₂ or GeSe₂ were fabricated. The two devices only showed positive photo responses. Neither of the devices showed non-volatile and negative photo-responsive features (Supplementary Fig. 26). This confirmed that the vdW heterostructure ReS₂/GeSe₂ layer is essential for non-volatile memory and positive/negative photoresponsivity. The band structure of the vdW heterostructure dominates the carrier generation, separation, and transportation. This is the foundation of 2D optoelectronic performances. Fermi level, E_C , and E_V were measured to get more insights into the working mechanism. The Fermi levels of ReS₂ and GeSe₂ were measured by the Kelvin probe force microscopy (KPFM)⁶⁹. The deduction of the Fermi level for ReS₂ and GeSe₂ was -5.135 eV and -5.031 eV, respectively (Supplementary Fig. 27e)⁷⁰. Besides, ultraviolet photoelectron spectroscopy (UPS) was utilized to measure the position of the valence band maximum (VBM), ionization energy, and work function of the ReS₂ and GeSe₂ flakes. The bandgap was deduced from the Tauc plot of the UV-visible optical spectroscopy (Supplementary Fig. 28a, d). The bandgap of ReS₂ and GeSe₂ were around 1.34 eV and 2.66 eV, respectively⁶. The Fermi levels of ReS₂ and GeSe₂ were 5.214 and 5.029 eV, which was consistent with the KPFM results (Supplementary Fig. 28b, e). The UPS binding energy profiles of ReS₂ (Supplementary Fig. 28c) flake and GeSe₂ (Supplementary Fig. 28f) can be used to calculate the energy difference between the valence band and the Fermi level^{71,72}. The VBMs of ReS₂ and GeSe₂ were -6.024 eV and

−6.030 eV, respectively. The CBM of ReS₂ (−4.7 eV)^{73,74} is lower than that of GeSe₂ (−3.3 eV)⁷⁵. The density functional theory (DFT) was employed to calculate the energy band structure of the ReS₂/GeSe₂ heterojunction (Fig. 3g)⁷⁶. The corresponding density of states (DOS) curves are presented (Supplementary Fig. 29). Based on the orbital character, the valence and conduction bands were exhibited in different colors ranging from red (orbitals contribution from GeSe₂) to blue (orbitals contribution from ReS₂)^{77,78}. The values of E_C and E_V were determined by the interlayer interaction strength. The GeSe₂ possessed a larger band gap compared to the ReS₂ counterpart (Fig. 3g). The conduction band offset at the interface was relatively big. While the valence band offset was small (Supplementary Fig. 30). The DFT simulation was consistent with the experimental results of KPFM and UPS. The band structure of ReS₂/GeSe₂ was identified by both experiments and the theoretical simulation, which was close to the reported results^{72,75}.

The I_{ds} - V_{gs} curves under different sweeping rates were measured to study the carrier's trapping and de-trapping processes (Supplementary Fig. 31). An obvious hysteresis loop of I_{ds} was obtained when the forward/backward sweeping gate voltages were applied. The mechanism was gate-voltage-controlled carrier's redistribution in the device (Supplementary Fig. 32)⁷⁹. The working mechanisms of PPC and NPC are schematically depicted (Fig. 3h to Fig. 3l). To achieve optical-controlled conductance modulation, a gate voltage of −10 V was applied. For the PPC behavior, the light (wavelength of 808 nm) generated excitons in the ReS₂ layer due to the strong absorption of ReS₂. At the initial state, the vacancy states on the GeSe₂ surface were occupied by electrons (Fig. 3h), which depleted the majority carriers of electrons in the ReS₂ channel. The device showed relatively low conductivity. The 808 nm light excited the electrons to the conduction band, generating electron-hole pairs in ReS₂ (Fig. 3i). The holes migrated to the GeSe₂ under the negative gate voltage of −10 V and neutralized with the trapped electrons (Fig. 3i). The electronic strength depleting the channels' carriers decreased due to less trapped electrons, resulting in higher conductivity (Fig. 3i). The high conductivity remained when the light was removed. Positive charged vacancies caused non-volatile PPC. When further applying 808 nm light, more electrons in the vacancy's states were neutralized, corresponding to higher conductivity (Fig. 3j). This explains why the conductance was modulated gradually, which was essential for ANNs implementing matrix-vector multiplication (MVM)⁸⁰. In comparison, the 405 nm light generated electron-hole pairs in the GeSe₂ layer. The excessive electrons inside the GeSe₂ were pushed to the surface of GeSe₂ and were trapped by vacancy defects (Fig. 3k). The majority carriers of electrons were depleted by the trapped electrons, leading to decreased conductivity. More 450 nm light pulses induce more trapped electrons, leading to lower conductivity (Fig. 3l). Although the 450 nm light may also generate electron-hole pairs in ReS₂. The screening effect from the trapped electron dominated the conductivity modulation. The similar theory has been reported in previous work^{81–83}. The ReS₂/GeSe₂ heterostructure has bi-axial optoelectronic properties due to in-plane anisotropic structures. This was the fundamentals for the PPC and NPC with polarimetric functions.

Moreover, the influence of the twist angles (the twist angle between the b-axis of ReS₂ and the b-axis of GeSe₂) on optoelectronic responses has been investigated. The twist angle in the twistronic optoelectronic devices was adjusted from 0° to 90° by in-situ rotating the ReS₂ layer (Supplementary Fig. 33). A typical optical microscopy image of the twistronic optoelectronic device with 60° was provided (Supplementary Fig. 34). The polarized light with 405 nm wavelength was used to modulate the optoelectronic properties. The linear polarization direction was fixed and was parallel with the b-axis of GeSe₂. The I_{ds} - V_{gs} curves with different twist angles between ReS₂ and GeSe₂ were measured (Supplementary Fig. 35). The suppression of current amplitude was obtained for all angles, corresponding to NPC

responses. A negligible difference was observed when changing the angle between ReS₂ and GeSe₂. This means that the alignment angle of anisotropic ReS₂ and GeSe₂ barely affected NPC responses. Trap states screening the gate electric field is the main reason for suppressed photocurrents (Fig. 3h–l). This is consistent with the previous report⁸⁴.

Biomimetic real-time navigation by OCPM arrays

OCPM machine vision systems are designed for multiple functions, including image sensing, polarimetric measurement, and optical-controlled synaptic weights. The sensory functions realize front-end image sensing, which is the input for high-level back-end cognitive tasks. On the other hand, the fully optical-controlled conductance represents the weight updating in ANNs. OCPM arrays can deploy deep learning algorithms for cognitive tasks. Moreover, the ability of polarimetric measurement can be used for navigation and anti-glare pattern recognition, which goes beyond traditional humanoid machine vision and revolutionizes interspecies-chimera machine vision.

Many animals (for example, honeybees) rely on the sun compass for spatial orientation. They can effectively identify directions even in poor weather (e.g. invisible sun, cloudy) by measuring the celestial polarization patterns, which cannot be done by human eyes⁸⁵. Honeybees are masters at real-time navigating to attractive flower patches with the help of polarized-light patterns. A scout honeybee uses waggle dance (waggles back and forth as moving forward in a straight line) on the honeycomb to transmit the location information to its nest-mates (Fig. 4a)⁸⁶. The waggle phase gives the distance information from their hive to the follower. The angle between the waggle segment's axis and the upwards of the honeycomb (a reference direction defined by honeybees living in the hive) represents the angle between the sun and the fly direction. The reason that a honeybee can navigate is that they can measure the polarized light in the sky. Even on cloudy days, they can steer correctly on the way to the target owing to inferring the sun's position by measuring the pattern of polarized light (Fig. 4b). The major components of polarization-vision pathways for identifying navigation maps are demonstrated (Supplementary Fig. 36a–c). The dorsal rim area (DRA) is sensitivity to polarized light. This can be realized by orthogonal positioned OCPM arrays for polarization measurements. Notably, polarization-sensitive synaptic plasticity can be mimicked by OCPM with both excitation and inhibition capabilities. The OCPM realizes fetterless, polarizer-free, and miniaturization for polarization navigation, avoiding bulky configurations with separated filters and polarizers. This demonstrates that OCPM is an excellent candidate building block for real-time navigation systems.

In the sky, the polarized sunlight is symmetrically distributed about the solar meridian (SM). The polarization direction (PD) is perpendicular to the direction of SM. Therefore, direction identification can be achieved by measuring the direction of SM or PD. As a proof-of-concept, the navigation accuracy was experimentally evaluated on a typical cloudy day. The OCPM was tested outdoors with natural skylights. No packaging processing was implemented. The device exhibited excellent resilience in ambient environments. The test setup is shown in Fig. 4c. The angle-dependent I_{ds} was measured (Fig. 4d, e). The interval angle for each test was 15° with respect to the reference direction of north. The b-axis of ReS₂ pointing the north and south was defined as 0° (Supplementary Fig. 37). The detailed methodology can be found in Supplementary Note 1. The results showed angle-dependent current amplitudes. The device at HRS and LRS both showed polarization sensitivity. The reconfigurable electronic feature makes it more compatible with other ancillary circuits. Because the operation currents have different margins in HRS (0–0.2 nA) and LRS (20–94 nA) working models, which can have better compatibility with a wider range of peripheral circuits (Supplementary Fig. 38). The perceptive architecture of OCPM array coupling with algebraic analysis realizes navigation applications (Fig. 4f, Supplementary Note 1).

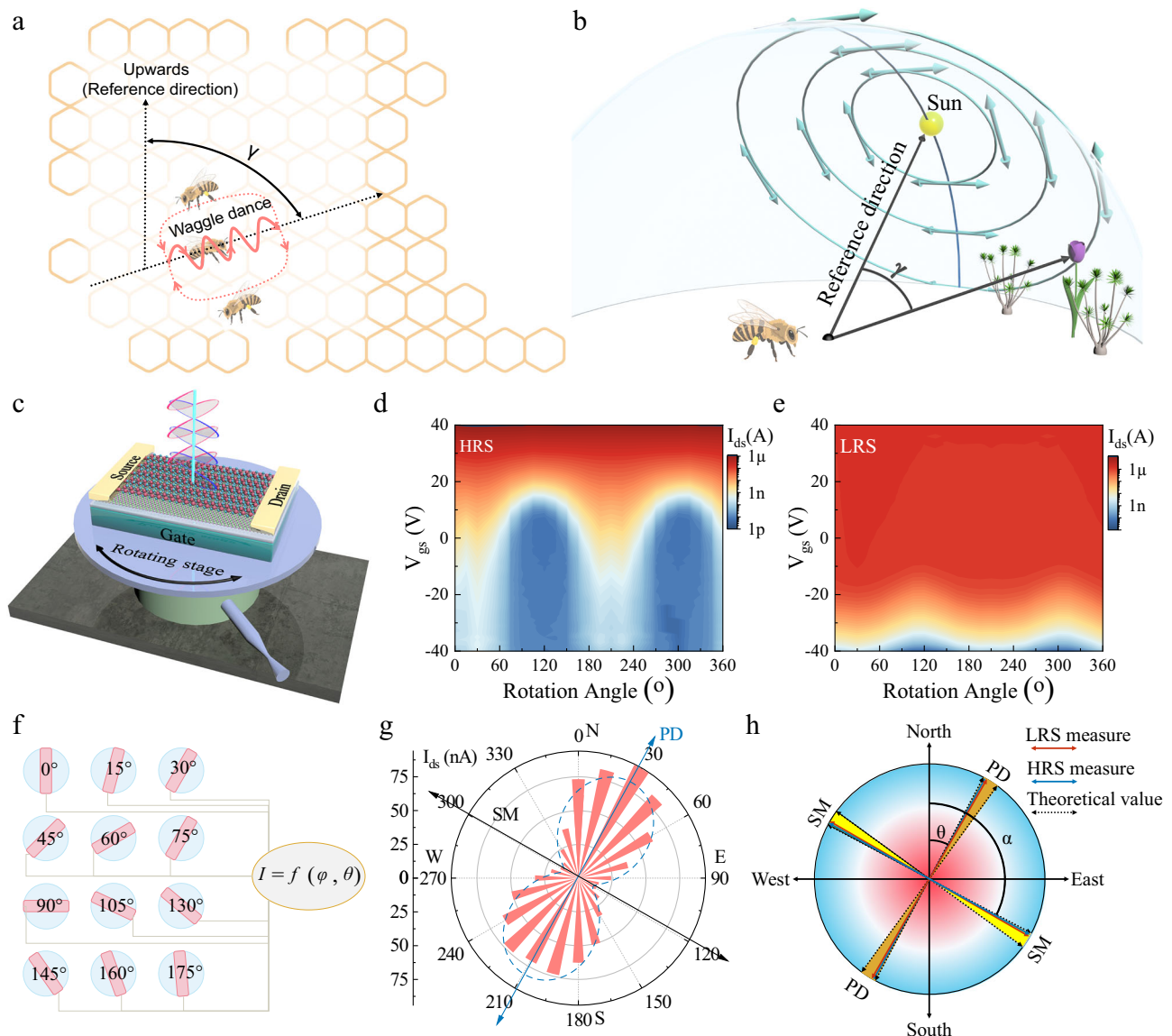


Fig. 4 | Biomimetic real-time navigation using OCPM arrays. **a** Schematic diagram of honeybee's waggle dance in the honeycomb, which tells watching bees the flower patch's location (direction and distance). **b** Schematic diagram of a honeybee flying toward the indicated flower patch using the sun as the reference. **c** Schematic diagram of the experimental setup for measuring celestial polarization patterns. **d** Polarization-dependent I_{ds} - V_{gs} mapping for the OCPM at HRS. ($V_{ds} = 1$ V).

e Polarization-dependent I_{ds} - V_{gs} mapping for the OCPM at LRS. ($V_{ds} = 1$ V). **f** The perceptive architecture of OCPM array for navigation. **g** The polar coordinate plot of angle-dependent I_{ds} at LRS. The black and blue arrows represent the PD and SM, respectively. The blue dashed line is the fitting result. (9.14–9.51 AM, Longitude of 113.91°, Latitude of 35.34°, March 12, 2023). **h** The real-time orientations of PD and SM at zenith. Experimentally measured results locate in the theoretical slot.

Typical polar coordinate plots of angle-dependent I_{ds} at LRS (Fig. 4g) and HRS (Supplementary Fig. 39) were measured. The experimentally measured SM angles were 119.3° (PD angle of 29.3°) and 119.6° (PD angle of 29.6°) under HRS and LRS working models respectively. The two figures (Fig. 4g and Supplementary Fig. 39) were very close with a relative deviation (RD) of merely 0.12% ($RD = |SM_{HRS} - SM_{LRS}| / (SM_{HRS} + SM_{LRS})$), demonstrating the consistency of the two working models. The experimental results were compared with the theoretical values (Fig. 4h). The north was employed as the reference direction (north was 0°). The evolution of solar azimuth angle over a day was calculated (Supplementary Figs. 40). The theoretical α was 118.8°–126.7° over the measuring time slot (9.14–9.51 AM), corresponding to the θ of 28.8°–36.7° (PD direction relative to the north direction). The red and blue arrows represent the measured results with the device at LRS and HRS respectively. The experimental values with OCPM were located right in the theoretical slot, demonstrating a high navigation accuracy and practical applications. Notably, the

presented system simplifies the system's complexity due to the filter-free and polarizer-free features⁸⁷.

Anti-glare pattern recognition by OCPM arrays

Human-bee chimera machine vision integrates polarimetry and cognitive recognition functions, which overmatch traditional neuromorphic vision systems. Reflected light from a surface (usually non-metallic) is partially polarized according to Fresnel's law⁸⁸. The reflected light is usually very strong, inducing glare spots that will distort visualized images and decrease cognitive accuracy in machine vision. Specifically, automatic vehicles and drones require real-time sensing and processing traffic information. Therefore, three major challenges for image processing in automatic machines are sensing and processing accuracy, computing speed, and energy consumption. However, reflective materials used in buildings, advertising boards with smooth surfaces, and a body of water produce lots of glare spots. This will exacerbate the processing accuracy and increase the risk.

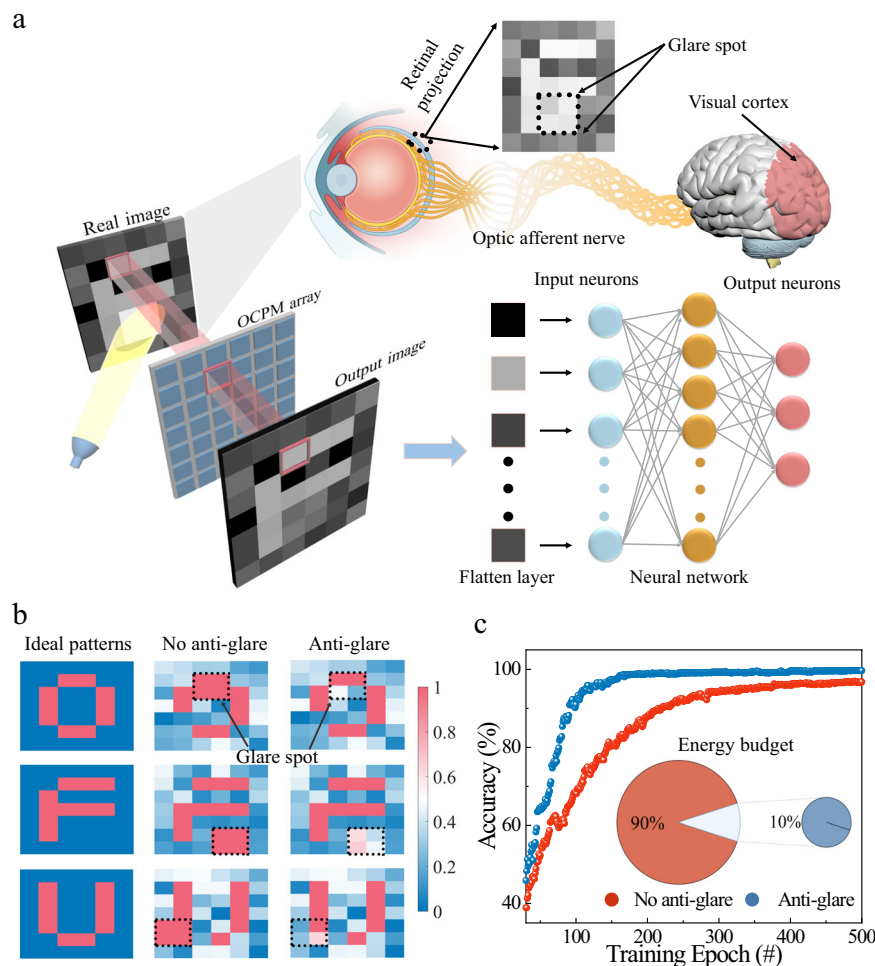


Fig. 5 | Anti-glare pattern recognition. **a** Schematic diagram of human eyes versus OCPM arrays processing patterns with glare spots. The OCPM array can effectively suppress the glare-spot-induced image distortion. Neuromorphic computing can be implemented by OCPM arrays. **b** Examples of ideal patterns, no anti-glare

processing, and the patterns with anti-glare processing with OCPM. **c** Comparison of pattern recognition accuracy with and without OCPM-based anti-glare processing. The inset shows the energy budgets. The anti-glare function significantly improved the interspecies-chimera computing efficiency.

Note, the formation of glare spots is because the reflected light is polarized light parallel to the surface. The polarimetric capabilities of OCPM can filter the polarized light and reduce the influence of glare spots. Besides, fully optic-controlled synapse can be used to build ANNs for cognitive pattern recognition¹⁶. An anti-glare machine vision can be developed by integrating polarimetric and synaptic functions.

The comparison between human vision systems and OCPM-based honeybee-chimera machine vision is illustrated (Fig. 5a). A real image with glare spots is sensed by photoreceptors in human eyes. The image is projected on the retina. Human eyes cannot reduce the intensity of glare spots on images. The projected image reserves the glare spot that distorts the picture of the letter “F” (on the top of Fig. 5a). The image will then be transformed into the visual cortex via optic afferent nerves for cognitive processing. The remained spot glare will influence the processing accuracy due to the distortion and partial-missing of the image. In comparison, the impact of spot glare can be obviously suppressed with the OCPM array thanks to the polarimetric ability (the letter “F” shown in the middle of Fig. 5a). Importantly, the OCPM array can perform as ANNs implementing deep learning for cognitive tasks, mimicking the function of the visual cortex.

As a proof of concept, the excellence of anti-glare pattern recognition with OCPM has been presented. A dataset with three letters of “O”, “F”, and “U” with 6×7 pixels was adopted for the training and testing. The scale of each pixel was 0–1. Ideal patterns (no background noise and glare-spot-like noise), no anti-glare patterns, and

anti-glare patterns are shown (Fig. 5b). The background noise was randomly generated in a margin of 0–0.5. It was assumed that the Brewster angle was reached for the reflected light, indicating the reflected light was linearly polarized⁸⁹. The pixel in the glare spot was considered as “1”, and the glare spot size was 2×2 . The suppression degree of glare spots with OCPM was determined by the sensitivity of linearly polarized lights. The dichroic ratio of ~6.4 under pulsed operation was employed based on experimental results. The noise due to glare spots decreased to the 1/6.4 of original values with the anti-glare processing based on the dichroic ratio. The glare spots were effectively decreased (Fig. 5b). The patterns were fed into an artificial network for training and recognition. More detailed simulation details are presented in (Supplementary Note 2, Figs. 41–44). The pattern recognition accuracies with and without OCPM-based anti-glare processing were calculated (Fig. 5c). The anti-glare processing can improve the accuracy compared to the no anti-glare counterparts (Fig. 5c). The recognition accuracy plots for 9 running cycles were calculated to implement statistics analysis (Supplementary Fig. 45). The same conclusion can be obtained that the anti-glare interspecies-chimera machine vision showed better performances despite minor differences among different running cycles. The statistical comparison of training efficiency with and without anti-glare abilities was demonstrated (Supplementary Fig. 46). The average values were summarized in (Supplementary Table 2). To get the recognition accuracy of 70%, 57 and 99 training epochs were required for with and without anti-glare

functions respectively (Supplementary Table 2). 2410 epochs were needed to get 99% accuracy for the humanoid neuromorphic machine vision without anti-glare functions (Supplementary Table 2). Remarkably, the anti-glare function can significantly reduce the training epochs to merely 245 using interspecies-chimera machine vision, almost one magnitude of difference (Supplementary Table 2). The ratio of improvement (RoI) was as high as nearly 90% (Supplementary Table 2) which was much higher than previous reported results with image pre-processing abilities¹². Besides, the training processing is the most energy-intensive step which is determined by neural network size, dataset size, training epochs, etc. As we fixed other variables (network size, dataset size, etc.) during the training process. The training epochs qualitatively reflect the significantly improved energy efficiency (Inset of Fig. 5c). The training energy consumption was reduced to 11.4% aided by the anti-glare abilities (Inset of Fig. 5c). The abovementioned anti-glare pattern recognition assumed that the OCPM was perpendicular to the polarized light reflection. The randomness of polarization directions may influence the effectiveness of the anti-glare recognition. In the system-level design, a polarization measurement component is required to make sure that OCPM is perpendicular to the polarized reflected light. Notably, our OCPM can identify the polarization of the reflected light, which can potentially make the whole system simplified. This work focuses on device-level development. It is a proof of concept that our device can improve computing efficiency. The relative angle (the angle between the polarized light reflection and device orientation) impacts the recognition accuracy (Supplementary Fig. 47). The recognition accuracy improved by different margins under different angles due to the anti-glare function. Therefore, even without the polarization calibration components, the device can still surpass traditional technology. The OCPM equipped interspecies-chimera machine vision with the anti-glare function, which can effectively improve computing speed with significant lower energy consumption. This technique has a bright future for energy-efficient interspecies-chimera computing systems.

We have reported an interspecies-chimera machine vision by integrating the polarimetric function of honeybees and the intelligence of human beings. The device based on a van der Waals heterostructure (ReS₂/GeSe₂) provides polarization sensitivity, nonvolatility, and positive/negative photoconductance simultaneously. The polarimetric measurement can identify celestial polarizations for real-time navigation. Meanwhile, the anti-glare recognition with polarimetry improved one magnitude of energy efficiency compared to the traditional neuromorphic machine vision counterpart. This technique will boost the applications in autonomous vehicles, medical diagnoses, intelligent robotics, and navigation without satellite-based GPS systems etc.

Methods

Device fabrications: Multilayer GeSe₂ was exfoliated from bulk crystal using Nitto tape and directly transferred onto a highly p-doped silicon substrate that was covered by silicon dioxide (90 nm). ReS₂ was mechanically exfoliated and transferred onto the GeSe₂ flake, which was assisted by an aligned transfer system equipped with an optical microscope (Shanghai Onway Technology Co., Ltd.). After preparing the heterostructures, electrodes with 5 nm Cr/45 nm Au were prepared by maskless lithography (Tuotuo Technology (Suzhou) Co., Ltd.), thermal evaporation, and lift-off techniques. The GeSe₂ holder can be rotated to change the alignment direction. Meanwhile, the ReS₂ layer can be picked up or dropped down at desired positions with the help of polyvinyl alcohol (PVA) stamp. This can fabricate different alignment angles of ReS₂/GeSe₂.

Material characterizations: The thickness and morphology were observed by optical microscope (Nikon LV100POL), atomic force microscope (Bruker ContourGT). The optical properties were measured by a micro UV-Vis spectrophotometer (Jasco MSV-5000). The

anisotropic Raman spectra were obtained using a LabRAM-HR Evolution Raman spectrometer with an excitation wavelength of 532 nm. The HAADF images and FFT patterns were measured by Spectra Ultra aberration corrected Scanning Transmission Electron Microscope (Thermo Scientific Spectra 300 S/TEM). Ultraviolet photoelectron spectroscopy (UPS) measurements were performed with a monochromated photon energy of 21.21 eV (He^I) through a toroidal mirror monochromator (SPECS GmbH). The chamber of base pressure was lower than 5×10^{-10} mbar. Kelvin probe force microscopy (KPFM) measurements were carried out in Amplitude Modulation mode (AM-KPFM) using a conductive tip.

Optoelectronic measurement: The optoelectrical measurements were carried out on a probe station (Linkam, HFS350EV-PB4) equipped with a semiconductor characterization system (Keysight, B1500A). A 405-nm laser (TEM-F-405, Cnilaser), 670-nm laser (MDL-III-670-SM, Cnilaser), and 808-nm laser (TEM-F-808, Cnilaser) were used as light sources. The time response photocurrents were tested by switching the light on/off with an electronic shutter. Linear polarization-resolved photodetection was carried out with the help of a polarizer and a half-wave plate. All the measurements were carried out at room temperature in an ambient environment.

Density Functional Theory calculations: First-principles calculations were performed using the projector-augmented wave (PAW) method as implemented in the Vienna ab initio simulation package (VASP). The Perdew-Burke-Ernzerhofer (PBE) formula within the generalized gradient approximation (GGA) was used to describe the exchange correlation. The DFT-D2 method of Grimme was used to describe the vdW heterostructure interaction. The vacuum region of 20 Å was set along the x direction to avoid virtual interaction between adjacent images for 2D vdW heterostructure. The cutoff energy was 450 eV. All the structures were relaxed until the forces on all unconstrained atoms were smaller than 0.01 eV/Å, and the total energy convergence criterion was 10^{-4} eV.

Simulation of anti-glare pattern recognition: The code was written with MATLAB. Three-layered ANN was utilized with an input layer (42 neurons), a hidden layer (20 neurons), and an output layer (3 neurons). The training images have 6×7 pixels. The training and recognition processes were based on the backpropagation (BP) algorithm. The activation function was Sigmoid. A more detailed description can be found in the supplementary document (Supplementary Note 2).

Data availability

The authors declare that all data generated in this study are provided in the Supplementary Information/Source Data file. Source data are provided with this paper.

Code availability

All the DFT calculations were performed using the commercial software VASP. All the input and output files of the calculations are available per request.

References

- Charan, A., Karthik Chowdary, C. & Komal, P. The Future of Machine Vision in Industries- A systematic review. *IOP Conf. Ser. Mater. Sci. Eng.* **1224**, 012027 (2022).
- Li, C. et al. Analogue signal and image processing with large memristor crossbars. *Nat. Electron* **1**, 52–59 (2018).
- Zhang, Z. et al. All-in-one two-dimensional retinomorphic hardware device for motion detection and recognition. *Nat. Nanotechnol.* **17**, 27–32 (2022).
- Fu, X. et al. Graphene/MoS₂-xOx/graphene photomemristor with tunable non-volatile responsivities for neuromorphic vision processing. *Light Sci. Appl.* **12**, 39 (2023).
- Jiang, T. et al. Tetrachromatic vision-inspired neuromorphic sensors with ultraweak ultraviolet detection. *Nat. Commun.* **14**, 2281 (2023).

6. Guo, T. et al. Broadband Optoelectronic Synapse Enables Compact Monolithic Neuromorphic Machine Vision for Information Processing. *Adv. Funct. Mater.* **33**, 2303879 (2023).
7. Mehonic, A. & Kenyon, A. J. Brain-inspired computing needs a master plan. *Nature* **604**, 255–260 (2022).
8. Xia, Q. & Yang, J. J. Memristive crossbar arrays for brain-inspired computing. *Nat. Mater.* **18**, 309–323 (2019).
9. Kim, J. H., Stolte, M. & Würthner, F. Wavelength and Polarization Sensitive Synaptic Phototransistor Based on Organic n-type Semiconductor/Supramolecular J-Aggregate Heterostructure. *ACS Nano* **16**, 19523–19532 (2022).
10. Han, L. et al. Desktop lighting for comfortable use of a computer screen. *Work* **68**, S209–S221 (2021).
11. Wang, W. et al. Neuromorphic sensorimotor loop embodied by monolithically integrated, low-voltage, soft e-skin. *Science* **380**, 735–742 (2023).
12. Zhou, F. et al. Optoelectronic resistive random access memory for neuromorphic vision sensors. *Nat. Nanotechnol.* **14**, 776–782 (2019).
13. Liao, F. et al. Bioinspired in-sensor visual adaptation for accurate perception. *Nat. Electron.* **5**, 84–91 (2022).
14. Wang, X. et al. Vertically integrated spiking cone photoreceptor arrays for color perception. *Nat. Commun.* **14**, 3444 (2023).
15. Cai, Y. et al. Broadband Visual Adaption and Image Recognition in a Monolithic Neuromorphic Machine Vision System. *Adv. Funct. Mater.* **33**, 2212917 (2023).
16. Wang, C.-Y. et al. Gate-tunable van der Waals heterostructure for reconfigurable neural network vision sensor. *Sci. Adv.* **6**, eaba6173 (2020).
17. Pi, L. et al. Broadband convolutional processing using band-alignment-tunable heterostructures. *Nat. Electron.* **5**, 248–254 (2022).
18. Euler, T., Haverkamp, S., Schubert, T. & Baden, T. Retinal bipolar cells: elementary building blocks of vision. *Nat. Rev. Neurosci.* **15**, 507–519 (2014).
19. Wolff, L. B. Polarization vision: a new sensory approach to image understanding. *Image Vis. Comput.* **15**, 81–93 (1997).
20. Saidi, I. S., Jacques, S. L. & Tittel, F. K. Mie and Rayleigh modeling of visible-light scattering in neonatal skin. *Appl. Opt.* **34**, 7410 (1995).
21. Krapp, H. G. Polarization Vision: How Insects Find Their Way by Watching the Sky. *Curr. Biol.* **17**, R557–R560 (2007).
22. Perumal, P. S. et al. An insight into crash avoidance and overtaking advice systems for Autonomous Vehicles: A review, challenges and solutions. *Eng. Appl. Artif. Intell.* **104**, 104406 (2021).
23. Wang, Q. H., Kalantar-Zadeh, K., Kis, A., Coleman, J. N. & Strano, M. S. Electronics and optoelectronics of two-dimensional transition metal dichalcogenides. *Nat. Nanotech.* **7**, 699–712 (2012).
24. Li, L. et al. Emerging in-plane anisotropic two-dimensional materials. *InfoMat* **1**, 54–73 (2019).
25. Nicholls, L. H. et al. Ultrafast synthesis and switching of light polarization in nonlinear anisotropic metamaterials. *Nat. Photon.* **11**, 628–633 (2017).
26. Wang, X. et al. Polarization-Sensitive Halide Perovskites for Polarized Luminescence and Detection: Recent Advances and Perspectives. *Adv. Mater.* **33**, 2003615 (2021).
27. Pan, J. et al. Anisotropic charge trapping in phototransistors unlocks ultrasensitive polarimetry for bionic navigation. *Nat. Commun.* **13**, 6629 (2022).
28. Zhu, K. et al. Hybrid 2D–CMOS microchips for memristive applications. *Nature* **618**, 57–62 (2023).
29. Liu, C. et al. Two-dimensional materials for next-generation computing technologies. *Nat. Nanotechnol.* **15**, 545–557 (2020).
30. Sangwan, V. K. et al. Multi-terminal memtransistors from polycrystalline monolayer molybdenum disulfide. *Nature* **554**, 500–504 (2018).
31. Mennel, L. et al. Ultrafast machine vision with 2D material neural network image sensors. *Nature* **579**, 62–66 (2020).
32. Pam, M. E. et al. Interface Modulated Resistive Switching in Mo Irradiated ReS₂ for Neuromorphic Computing. *Adv. Mater.* **34**, 2202722 (2022).
33. Soliman, M. et al. Photoferroelectric All-van-der-Waals Heterostructure for Multimode Neuromorphic Ferroelectric Transistors. *ACS Appl. Mater. Interfaces* **15**, 15732–15744 (2023).
34. Xie, D. et al. Porous Metal–Organic Framework/ReS₂ Heterojunction Phototransistor for Polarization Sensitive Visual Adaptation Emulation. *Adv. Mater.* **35**, 2212118 (2023).
35. Xie, D. et al. Polarization-perceptual anisotropic two-dimensional ReS₂ neuro-transistor with reconfigurable neuromorphic vision. *Mater. Horiz.* **9**, 1448–1459 (2022).
36. Wu, D. et al. Wafer-scale synthesis of wide bandgap 2D GeSe₂ layers for self-powered ultrasensitive UV photodetection and imaging. *Nano Energy* **104**, 107972 (2022).
37. Yan, Y. et al. Direct Wide Bandgap 2D GeSe₂ Monolayer toward Anisotropic UV Photodetection. *Adv. Optical Mater.* **7**, 1900622 (2019).
38. Zhao, M., Li, R. & Xue, J. Atomic bridge memristor based on silver and two-dimensional GeSe. *AIP Adv.* **10**, 045003 (2020).
39. Rahman, M., Davey, K. & Qiao, S.-Z. Advent of 2D Rhenium Disulfide (ReS₂): Fundamentals to Applications. *Adv. Funct. Mater.* **27**, 1606129 (2017).
40. Sutter, E., French, J. S. & Sutter, P. Germanium Diselenide Ribbons with Orthorhombic Crystal Structure. *Nano Lett.* **22**, 7952–7958 (2022).
41. Wang, J. et al. Polarized Light-Emitting Diodes Based on Anisotropic Excitons in Few-Layer ReS₂. *Adv. Mater.* **32**, 2001890 (2020).
42. Yang, Y. et al. Air-Stable In-Plane Anisotropic GeSe₂ for Highly Polarization-Sensitive Photodetection in Short Wave Region. *J. Am. Chem. Soc.* **140**, 4150–4156 (2018).
43. Ghimire, G. et al. Doping-Mediated Lattice Engineering of Monolayer ReS₂ for Modulating In-Plane Anisotropy of Optical and Transport Properties. *ACS Nano* **15**, 13770–13780 (2021).
44. Wang, X. et al. Experimental Evidence of Anisotropic and Stable Charged Excitons (Trions) in Atomically Thin 2D ReS₂. *Adv. Funct. Mater.* **29**, 1905961 (2019).
45. Liu, F. et al. Highly Sensitive Detection of Polarized Light Using Anisotropic 2D ReS₂. *Adv. Funct. Mater.* **26**, 1169–1177 (2016).
46. Yumigeta, K. et al. The synthesis of competing phase GeSe and GeSe₂ 2D layered materials. *RSC Adv.* **10**, 38227–38232 (2020).
47. Li, X. et al. Review of Anisotropic 2D Materials: Controlled Growth, Optical Anisotropy Modulation, and Photonic Applications. *Laser Photonics Rev.* **15**, 2100322 (2021).
48. Xu, X. et al. In-Plane Anisotropies of Polarized Raman Response and Electrical Conductivity in Layered Tin Selenide. *ACS Appl. Mater. Interfaces* **9**, 12601–12607 (2017).
49. Loudon, R. The Raman effect in crystals. *Adv. Phys.* **13**, 423–482 (1964).
50. Zhou, X. et al. Highly Anisotropic GeSe Nanosheets for Phototransistors with Ultrahigh Photoresponsivity. *Adv. Sci.* **5**, 1800478 (2018).
51. Dasgupta, A., Yang, X. & Gao, J. Naturally occurring van der Waals heterostructure lengenbachite with strong in-plane structural and optical anisotropy. *npj 2D Mater. Appl.* **5**, 1–13 (2021).
52. Guo, Z. et al. Controllable growth of large-area monolayer ReS₂ flakes by chemical vapor deposition. *J. Mater. Sci: Mater. Electron* **30**, 15042–15053 (2019).
53. Lin, Y.-C. et al. Single-Layer ReS₂: Two-Dimensional Semiconductor with Tunable In-Plane Anisotropy. *ACS Nano* **9**, 11249–11257 (2015).
54. Akkanen, S.-T. M., Fernandez, H. A. & Sun, Z. Optical Modification of 2D Materials: Methods and Applications. *Adv. Mater.* **34**, 2110152 (2022).
55. Chen, Y. et al. All Two-dimensional-Integration-Type Optoelectronic Synapse Mimicking Visual Attention Mechanism for Multi Target Recognition. *Adv. Funct. Mater.* **33**, 2209781 (2023).

56. Ahmed, T. et al. Fully Light-Controlled Memory and Neuromorphic Computation in Layered Black Phosphorus. *Adv. Mater.* **33**, 2004207 (2021).
57. Pezeshki, A. et al. Static and Dynamic Performance of Complementary Inverters Based on Nanosheet α -MoTe₂ p-Channel and MoS₂ n-Channel Transistors. *ACS Nano* **10**, 1118–1125 (2016).
58. Li, S. et al. A High-Performance In-Memory Photodetector Realized by Charge Storage in a van der Waals MISFET. *Adv. Mater.* **34**, 2107734 (2022).
59. Shan, X. et al. Plasmonic Optoelectronic Memristor Enabling Fully Light-Modulated Synaptic Plasticity for Neuromorphic Vision. *Adv. Sci.* **9**, 2104632 (2022).
60. Cheng, Z., Ríos, C., Pernice, W. H. P., Wright, C. D. & Bhaskaran, H. On-chip photonic synapse. *Sci. Adv.* **3**, e1700160 (2017).
61. Chang, C. et al. Mitigating Asymmetric Nonlinear Weight Update Effects in Hardware Neural Network Based on Analog Resistive Synapse. *IEEE J. Emerg. Sel. Top. Circuits Syst.* **8**, 116–124 (2018).
62. Yeon, H. et al. Alloying conducting channels for reliable neuromorphic computing. *Nat. Nanotechnol.* **15**, 574–579 (2020).
63. Fuller, E. J. et al. Li-Ion Synaptic Transistor for Low Power Analog Computing. *Adv. Mater.* **29**, 1604310 (2017).
64. van de Burgt, Y. et al. A non-volatile organic electrochemical device as a low-voltage artificial synapse for neuromorphic computing. *Nat. Mater.* **16**, 6 (2017).
65. Burr, G. W. et al. Experimental Demonstration and Tolerancing of a Large-Scale Neural Network (165 000 Synapses) Using Phase-Change Memory as the Synaptic Weight Element. *IEEE Trans. Electron Devices* **62**, 3498–3507 (2015).
66. Eichler, K. et al. The complete connectome of a learning and memory centre in an insect brain. *Nature* **548**, 175–182 (2017).
67. Xue, M., Atallah, B. V. & Scanziani, M. Equalizing excitation–inhibition ratios across visual cortical neurons. *Nature* **511**, 596–600 (2014).
68. Wang, M. et al. New Approach to Low-Power-Consumption, High-Performance Photodetectors Enabled by Nanowire Source-Gated Transistors. *Nano Lett.* **22**, 9707–9713 (2022).
69. Melitz, W., Shen, J., Kummel, A. C. & Lee, S. Kelvin probe force microscopy and its application. *Surf. Sci. Rep.* **66**, 1–27 (2011).
70. Palermo, V., Palma, M. & Samori, P. Electronic Characterization of Organic Thin Films by Kelvin Probe Force Microscopy. *Adv. Mater.* **18**, 145–164 (2006).
71. Jiang, X. et al. Ultra-high open-circuit voltage of tin perovskite solar cells via an electron transporting layer design. *Nat. Commun.* **11**, 1245 (2020).
72. Huang, F. et al. The influence of interfacial tensile strain on the charge transport characteristics of MoS₂ -based vertical heterojunction devices. *Nanoscale* **8**, 17598–17607 (2016).
73. Shim, J. et al. Phosphorene/rhenium disulfide heterojunction-based negative differential resistance device for multi-valued logic. *Nat. Commun.* **7**, 13413 (2016).
74. Srivastava, P. K. et al. Van der Waals Broken-Gap p–n Heterojunction Tunnel Diode Based on Black Phosphorus and Rhenium Disulfide. *ACS Appl. Mater. Interfaces* **11**, 8266–8275 (2019).
75. Yao, J. et al. Gate induced charge transfer and hysteresis enlargement in MoS₂/GeSe₂ vertical heterostructures. *J. Mater. Chem. C* **9**, 8213–8219 (2021).
76. Sham, L. J. & Schlüter, M. Density-Functional Theory of the Energy Gap. *Phys. Rev. Lett.* **51**, 1888–1891 (1983).
77. Shokri, A. & Yazdani, A. Band alignment engineering, electronic and optical properties of Sb/PtTe₂ van der Waals heterostructure: effects of electric field and biaxial strain. *J. Mater. Sci.* **56**, 5658–5669 (2021).
78. Tongay, S. et al. Tuning Interlayer Coupling in Large-Area Heterostructures with CVD-Grown MoS₂ and WS₂ Monolayers. *Nano Lett.* **14**, 3185–3190 (2014).
79. Shi, W. et al. Reversible writing of high-mobility and high-carrier-density doping patterns in two-dimensional van der Waals heterostructures. *Nat. Electron* **3**, 99–105 (2020).
80. Chai, Y. In-sensor computing for machine vision. *Nature* **579**, 32–33 (2020).
81. Pan, X. et al. Parallel perception of visual motion using light-tunable memory matrix. *Sci. Adv.* **9**, eadi4083 (2023).
82. Wang, S. et al. Nonvolatile van der Waals heterostructure phototransistor for encrypted optoelectronic logic circuit. *ACS Nano* **16**(3), 4528–4535 (2022).
83. Wu, E. et al. Dynamically controllable polarity modulation of MoTe₂ field-effect transistors through ultraviolet light and electrostatic activation. *Sci. Adv.* **5**, eaav3430 (2019).
84. Wang, Y. et al. Negative Photoconductance in van der Waals Heterostructure-Based Floating Gate Phototransistor. *ACS Nano* **12**, 9513–9520 (2018).
85. Labhart, T. & Meyer, E. P. Detectors for polarized skylight in insects: a survey of ommatidial specializations in the dorsal rim area of the compound eye. *Microsc. Res. Tech.* **47**, 368–379 (1999).
86. Srinivasan, M. V. Honeybee navigation. *Curr. Biol.* **13**, R894 (2003).
87. Kosuge, A., Yu, L., Hamada, M., Matsuo, K. & Kuroda, T. A Deep Metric Learning-Based Anomaly Detection System for Transparent Objects Using Polarized-Image Fusion. *IEEE Open J. Ind. Electron. Soc.* **4**, 205–213 (2023).
88. Xi, J.-Q. et al. Optical thin-film materials with low refractive index for broadband elimination of Fresnel reflection. *Nat. Photon* **1**, 176–179 (2007).
89. Hönig, D. & Möbius, D. Reflectometry at the Brewster angle and Brewster angle microscopy at the air-water interface. *Thin Solid Films* **210–211**, 64–68 (1992).

Acknowledgements

Y.A.W. thanks the funding from the Tang Family Chair professorship. Y.Y. thanks the funding supported by the Natural Science Foundation of China under Grant No.61804047. Scanning Transmission Electron microscopy was performed at the Canadian Centre for Electron Microscopy (also supported by NSERC and other government agencies). The computing resource for Density Functional Theory (DFT) calculations was supported by high-performance computing center (HPCC) of Henan Normal University. We would like to acknowledge the Zhongming Wei and Kexin He for their help on the Kelvin probe force microscopy (KPFM) measurement. The support from Iqbal Preet Singhd on the device simulation is also acknowledged.

Author contributions

T.G., Y.Y., Y.A.W. conceived the project. Y.A.W., Y.Y. supervised the project. T.G., Y.Y. carried out the device measurements, materials characterizations, and neuromorphic computing. S.L. assisted with the materials characterizations. T.G., Y.Y., and Y.A.W. wrote the manuscript. Y.N.Z., W.D.L. provided suggestions. All authors made comments and revised the manuscript.

Competing interests

The authors declare the following competing interests: T.G., Y.Y., Y.A.W. have filed a patent application on this technology related to this optical controlled polarimetry memtransistor attached with polarimetry for real-time navigation and anti-glare pattern recognition (US Patent application number 63/545,001). The remaining authors declare no competing interests.

Additional information

Supplementary information The online version contains supplementary material available at <https://doi.org/10.1038/s41467-024-51178-z>.

Correspondence and requests for materials should be addressed to Yong Yan or Yimin A. Wu.

Peer review information *Nature Communications* thanks the anonymous reviewers for their contribution to the peer review of this work. A peer review file is available.

Reprints and permissions information is available at <http://www.nature.com/reprints>

Publisher's note Springer Nature remains neutral with regard to jurisdictional claims in published maps and institutional affiliations.

Open Access This article is licensed under a Creative Commons Attribution-NonCommercial-NoDerivatives 4.0 International License, which permits any non-commercial use, sharing, distribution and reproduction in any medium or format, as long as you give appropriate credit to the original author(s) and the source, provide a link to the Creative Commons licence, and indicate if you modified the licensed material. You do not have permission under this licence to share adapted material derived from this article or parts of it. The images or other third party material in this article are included in the article's Creative Commons licence, unless indicated otherwise in a credit line to the material. If material is not included in the article's Creative Commons licence and your intended use is not permitted by statutory regulation or exceeds the permitted use, you will need to obtain permission directly from the copyright holder. To view a copy of this licence, visit <http://creativecommons.org/licenses/by-nc-nd/4.0/>.

© The Author(s) 2024